

Article

Petrogenesis of the Wadi El-Faliq Gabbroic Intrusion in the Central Eastern Desert of Egypt: Implications for Neoproterozoic Post-Collisional Magmatism Associated with the Najd Fault System

Shehata Ali ^{1,*}, Rainer Abart ², M. I. Sayyed ^{3,4,*}, Christoph A. Hauzenberger ⁵ and Mabrouk Sami ^{1,2}¹ Geology Department, Faculty of Science, Minia University, El-Minia 61519, Egypt² Department of Lithospheric Research, University of Vienna, Althanstrasse 14, A-1090 Vienna, Austria³ Department of Physics, Faculty of Science, Isra University, Amman 11622, Jordan⁴ Department of Nuclear Medicine Research, Institute for Research and Medical Consultations (IRMC), Imam Abdulrahman bin Faisal University (IAU), P.O. Box 1982, Dammam 31441, Saudi Arabia⁵ Institute of Earth Sciences—NAWI Graz Geocenter, University of Graz, Universitaetsplatz 2, 8010 Graz, Austria

* Correspondence: shehata.ali@mu.edu.eg (S.A.); dr.mabualssayed@gmail.com (M.I.S.)

Abstract: The late Neoproterozoic gabbroic intrusion of the Wadi El-Faliq area in the central Eastern Desert of Egypt (north Arabian–Nubian Shield; henceforth, ANS) is a fresh, undeformed elliptical body elongated in a NW–SE trend following the main sinistral strike-slip faults of the Najd fault system. Mineralogical and geochemical evidence suggest that they were derived from hydrous tholeiitic mafic magmas with arc-like geochemical fingerprints resembling the post-collisional gabbroic intrusions in Saudi Arabia. Despite the arc-like signatures, their fresh and undeformed nature, together with the field relationships, indicates that the studied gabbroic intrusion post-dates the main collisional phase, supporting its emplacement after subduction ceased and during the post-collisional stage. As a result, the arc-like signatures were possibly transmitted from the earlier ANS subduction episode. Indeed, the high $(La/Sm)_N$, and negative-Nb and positive-Pb anomalies suggest contributions from subduction components. Lithospheric delamination was possibly facilitated by the Najd faults and shear zones formed during the post-orogenic crustal extension associated with the Pan-African orogenic collapse. The delamination process could have generated a rapid upwelling and melting of the asthenosphere mantle. The melt-rock reaction process likely played an important role in the genesis of the studied rocks through the interaction of the asthenosphere melts with lithosphere mantle rocks during ascent. The HREE fractionation suggests a probable mixing between melts from both spinel- and garnet-bearing peridotites. We suggest that the Wadi El-Faliq gabbroic intrusion was likely emplaced due to the stretching and thinning of the lithosphere during the extensional tectonism following the Pan-African orogeny.

Keywords: hornblende gabbro; post-collisional extension; arc-like magmatism; Najd fault system; central Eastern Desert; Egypt



Citation: Ali, S.; Abart, R.; Sayyed, M.I.; Hauzenberger, C.A.; Sami, M. Petrogenesis of the Wadi El-Faliq Gabbroic Intrusion in the Central Eastern Desert of Egypt: Implications for Neoproterozoic Post-Collisional Magmatism Associated with the Najd Fault System. *Minerals* **2023**, *13*, 10. <https://doi.org/10.3390/min13010010>

Academic Editors: Hossein Azizi and Dominique Gasquet

Received: 13 November 2022

Revised: 11 December 2022

Accepted: 20 December 2022

Published: 22 December 2022



Copyright: © 2022 by the authors. Licensee MDPI, Basel, Switzerland. This article is an open access article distributed under the terms and conditions of the Creative Commons Attribution (CC BY) license (<https://creativecommons.org/licenses/by/4.0/>).

1. Introduction

The Arabian–Nubian Shield (ANS) occupies the northern part of the East African orogen, which was formed between 900 and 530 Ma [1]. The ANS is mainly composed of juvenile Neoproterozoic crust formed by the protracted accretion of the island arcs [2–4]. This juvenile crust was sandwiched between the continental regions of East and West Gondwana. The continental collision occurred at 640–650 Ma following the accretion stage which is believed to have terminated at ~700 Ma [5]. The post-collision stage occurred between 630 and 580 Ma and was characterized by the emplacement of alkaline, calc-alkaline, and tholeiitic magmatism during the late Neoproterozoic time [6–9]. Studying

post-collisional magmatism in the ANS can help the understanding of the geodynamic processes causing the termination of collision and the beginning of extensional collapse. Moreover, it shows changes in the magma source regions related to such processes.

Mafic magmatism in the ANS was emplaced in various tectonic regimes [10–14]. Late Proterozoic mafic plutonic rocks represent a major group and a distinctive rock unit in the Egyptian Pan-African basement complex. They are classified into younger and older gabbroic rocks [15]. These rocks show different ages and there is no general agreement regarding their source origin and tectono-magmatic evolution. Egyptian gabbroic rocks, based on their geochemical signatures, comprise three different categories [10]; (1) metagabbro–diorite–tonalite assemblages represent the synorogenic (900–800 Ma) intrusions of I-type affinity and island-arc signature, (2) ophiolitic metagabbros (780–730 Ma) constitute an essential part of the obducted ophiolite complexes, and (3) fresh “younger” gabbros represent post-orogenic (655–570 Ma) intrusions [15,16]. The calc-alkaline island-arc (subduction-related) and ophiolitic metagabbros of tholeiitic character belong to the older gabbros that suffered regional metamorphism up to the lower amphibolite metamorphic facies [17,18]. Younger gabbros were intruded during the late Cordilleran stage, slightly before post-orogenic granitic intrusions [19]. The post-collisional stage in the ANS started at 610 Ma ago [20]. Based on numerous studies, the post-collisional setting is generally accepted as a proper context for the generation of the younger gabbros [8,15,16,19]. The transition from convergence to extensional tectonics occurred at ~600 Ma during the evolution of the ANS [21].

The Najd fault system (NFS) represents a complex set of late Neoproterozoic NW- and NE-trending strike-slip faults and ductile shear zones in the ANS [22]. The faults striking NW are dominant and sinistral, whereas those striking NE are rare and dextral. The Najd faults bordered the Meatiq and other gneissic domes in the Eastern Desert of Egypt were active between 615 and 585 Ma [23]. The sinistral strike-slip faults prevail across the Precambrian of Arabia and Egypt [24]. They formed due to a large zone of NW–SE trending crustal extension that was associated with the formation of the juvenile continental crust in the northernmost part of Afro-Arabia [24].

This study presents for the first time new geologic, mineralogical and bulk-rock geochemical data of fresh intrusive hornblende gabbroic rocks located at the Wadi El-Faliq area of the Eastern Desert of Egypt, which represents the northeasternmost part of the ANS. The data are used to understand the tectonic emplacement of the Neoproterozoic mafic magmatism in the ANS and to explain the nature of the mantle source and melting conditions.

2. Geologic Setting and Petrography

The Red Sea rifting separates the ANS into two plates: the Arabian Shield to the east and the Nubian Shield to the west (Figure 1a). The Neoproterozoic (900–550 Ma) and Phanerozoic mafic rocks constitute an essential component of the Egyptian basement complex, which occupies the northern part of the Nubian Shield [10–12,19,25].

The Neoproterozoic gabbroic rocks are broadly dispersed in the Egyptian Eastern Desert [15,17,18]. In most localities over the Eastern Desert, the younger gabbros are frequently intruded into the island-arc tonalites, trondhjemites and granodiorites (TTG) and intruded by post-collisional highly fractionated calc-alkaline to alkaline granitoid rocks [10,26]. In the ANS, post-collisional intrusions were emplaced during the Ediacaran period (~620–590 Ma) in the late stages of arc amalgamation [27,28]. The Phanerozoic gabbros commonly occur as a part of the alkaline ring complexes, which are widely distributed in the southern Eastern Desert [29].

The NW trending sinistral strike-slip faults of the NFS of Arabia and Egypt were developed due to the escape tectonics associated with the collisional stage and were active during ~630–560 Ma [24]. They permitted northward orogen-parallel extension because of the escaping of the ANS from the collision between East and West Gondwana. The movements on the Najd faults terminated mostly in the Early Cambrian [30].

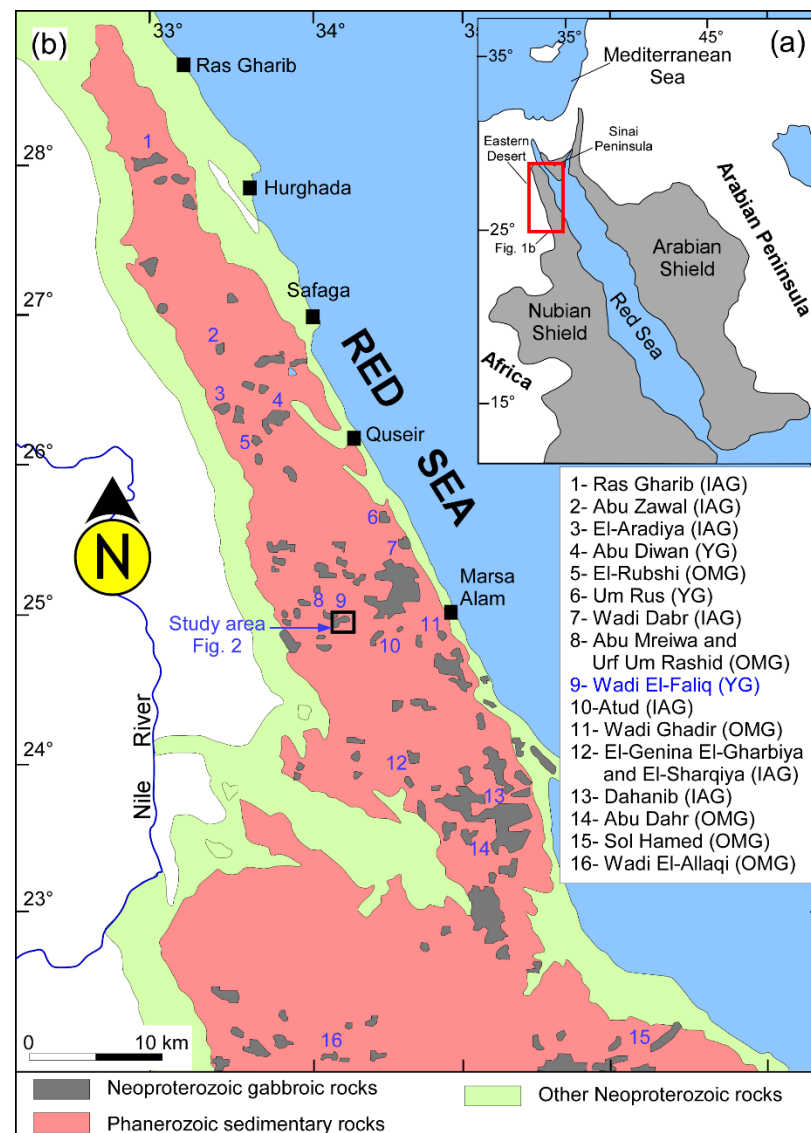


Figure 1. (a) A schematic general map of the ANS; (b) the distribution of various Neoproterozoic gabbroic rocks in the Eastern Desert of Egypt (modified after Abdelfadil et al. [15]). OMG: ophiolitic metagabbro; IAG: island arc gabbro; YG: younger gabbro.

The basement rocks of the El-Faliq area belong to the Precambrian rocks of the central Eastern Desert of Egypt as a part of the ANS. The area is covered by serpentinites, granites, and gabbros (Figure 2). The Wadi El-Faliq crosses the Mount Hommet Waggat and Mount El-Faliq granite masses and its surrounding terranes at the southern part of the central Eastern Desert of Egypt (Figure 2). Serpentinites are the oldest rock unit in the area; they are deformed and display lineation mostly trending N–NW. The granites are the most abundant rocks and include tonalite and granodiorite, along with the alkali-feldspar granite of Mount Hommet Waggat and Mount El-Faliq.

The tonalite and granodiorite, occurring beyond the limits of the mapped area, form small, isolated masses of low to moderate relief and exhibit dark gray, medium- to coarse-grained rocks containing mafic microgranular enclaves and xenoliths of older rocks [31]. They are weakly deformed and represent the older phase of granitic intrusions that were emplaced in the subduction setting [31]. The gabbroic intrusion forms a small semicircular mass with moderate to high relief at the extreme north of the Wadi El-Faliq and covers an area of about 4 km² NW of Mersa Alam city (Figure 1b). Although the granitoids have been

intensively investigated by several authors (e.g., [31–33]), the gabbroic rocks have received less attention and lack detailed mineralogical and geochemical studies. The gabbros are fresh and massive without any apparent foliation and show no evidence of deformation or metamorphism. These gabbros form an elliptical body elongated NW–SE (Figure 2a). They are dark green, medium- to coarse-grained rocks. Himmret Waggat post-collisional granites cover $\sim 50 \text{ km}^2$ with $\sim 1050 \text{ m}$ elevation above sea level and represent an elliptical ring of high relief elongated NW–SE [31]. Interestingly, both the intrusions of the El-Faliq gabbroic rocks and Himmret Waggat post-collisional granitic rocks follow the same NW–SE trend, which is probably related to the prevailing NW-trending sinistral strike-slip faults of the NFS of Egypt. The alkali-feldspar granites exhibit the characteristics of A-type granites and represent the youngest igneous activity in the study area [31,33]. They are fresh, medium- to coarse-grained rocks showing a massive appearance and distinctive pink to red color. They intruded the gabbros with sharp intrusive contacts (Figure 2); a characteristic feature of the younger (i.e., post-collisional) variety of gabbros. The area is dissected by numerous structurally controlled wadis filled with quaternary deposits.

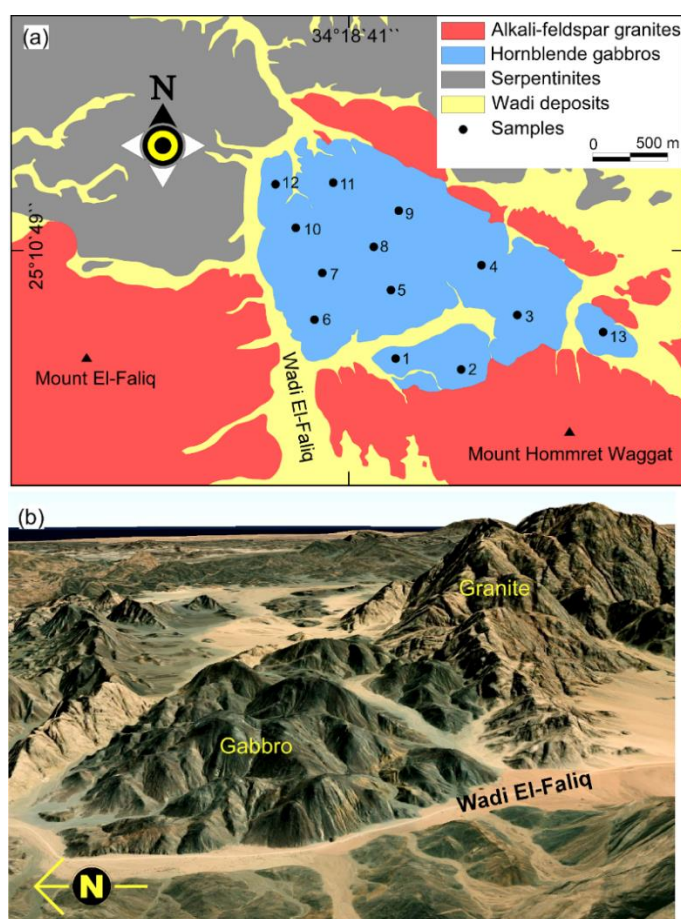


Figure 2. (a) A simplified geological map of the Wadi El-Faliq in the central Eastern Desert of Egypt showing the different lithologies in the area; and (b) a satellite image (ArcGIS Earth) of the northern side of the Wadi El-Faliq showing the relationship between gabbroic rocks and granites.

The studied hornblende gabbroic rocks are fresh, dark grey, medium- to coarse-grained, and exhibit a hypidiomorphic granular texture (Figure 3a–c). They are composed essentially of plagioclase and amphibole, with lesser amounts of biotite. Ilmenite, magnetite, chromite, titanite, apatite, and pyrite represent the accessory minerals. Very small amounts of chlorite and epidote represent the secondary products of amphibole alteration. Plagioclase is found as euhedral to subhedral crystals and exhibits polysynthetic twinning with rare compositional zoning. Amphibole occurs as subhedral prismatic and

platy crystals with occasional simple twinning and zoning. It sometimes contains inclusions of pyrite, plagioclase, and magnetite (Figure 3d–g). Biotite shows yellowish brown, pleochroic, subhedral prismatic crystals with characteristic parallel extinction and a bird’s eye pattern during extinction. It has perfect cleavage in one direction and occasionally contains magnetite inclusions (Figure 3c). The shred-like crystals of biotite are also observed. Pyrite is commonly hosted by amphiboles and sometimes rimmed by pentlandite (Figure 3d,e). Ilmenite and magnetite occur either as small subhedral crystals or as large euhedral crystals among and/or within plagioclase and amphibole (Figure 3f,g). Apatite is commonly found within amphibole as anhedral to subhedral small crystals (Figure 3c).

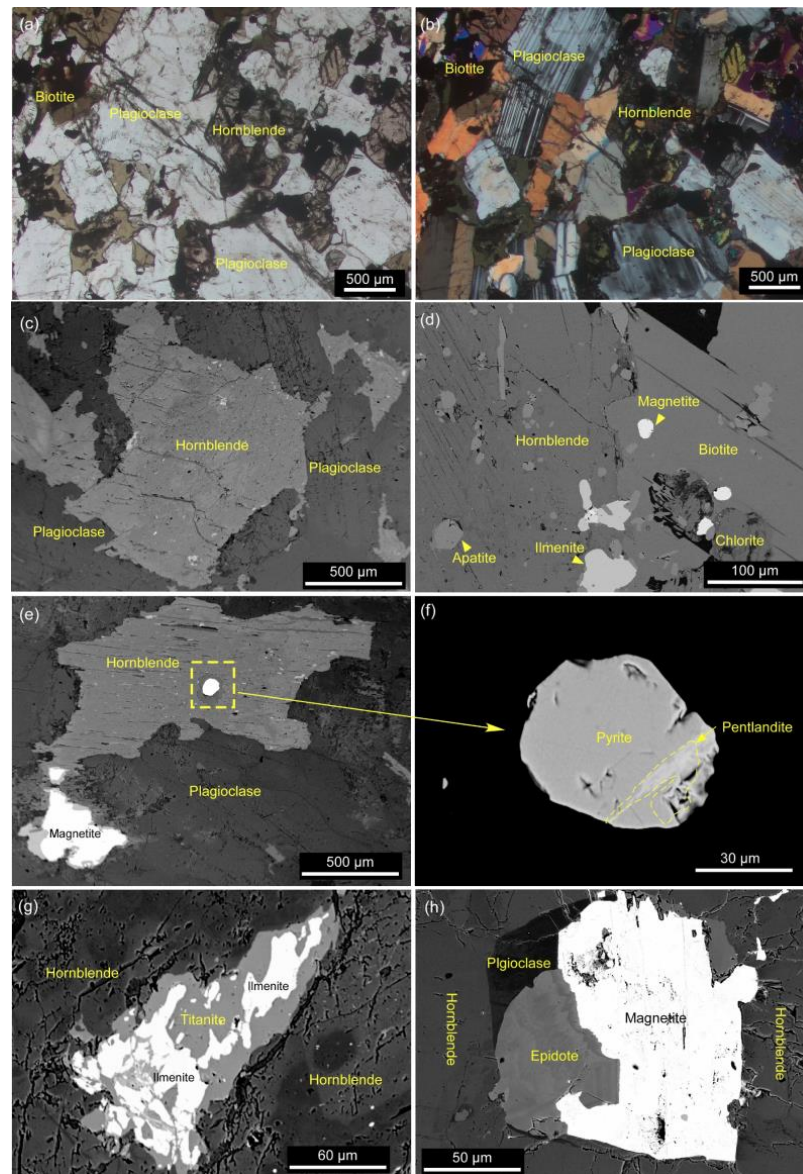


Figure 3. Photomicrographs and back-scattered electron (BSE) images from the Wadi El-Faliq hornblende gabbros showing: (a,b) aggregation of plagioclase, hornblende and biotite as major mineral components (a-PPL; b-XPL) in a typical hypidiomorphic texture; (c) association of coarse-grained hornblende and plagioclase, typical of granular hypidiomorphic texture; (d) intergrowth of hornblende and biotite, where both of them host inclusions of apatite and magnetite, respectively; (e) intergrowth of coarse-grained plagioclase, magnetite and hornblende where the later hosts pyrite; (f) subhedral pyrite penetrated by pentlandite; (g) intergrowth of ilmenite and titanite inside a coarse-grained hornblende crystal; and (h) aggregates of plagioclase, epidote and magnetite inside hornblende.

3. Analytical Techniques

For the mineralogical analysis, typical thin polished sections were prepared. The chemistry of the different minerals was probed using an electron microprobe (CAMECA SX100; University of Vienna, Vienna, Austria). The concentration of major, trace, and rare earth elements (REEs) in the gabbroic rock samples was measured using X-ray fluorescence (University of Vienna, Vienna, Austria) and an inductively coupled plasma mass spectrometer (ICP-MS; University of Graz, Graz, Austria). More details are provided in the Supplementary Material S1.

4. Results

4.1. Mineral Chemistry

The chemical compositions and chemical formulas of the essential (plagioclase, amphibole, and biotite), accessory (magnetite, ilmenite, titanite, and apatite) and secondary (chlorite and epidote) minerals in the gabbroic rocks are, respectively, listed in Supplementary Materials S2 (Tables S1–S8).

Plagioclase feldspars are mostly calcic ($\text{CaO} = 7.63\text{--}13.55$ wt.%; Supplementary Table S1) and range in composition from andesine to labradorite ($\text{An}_{41\text{--}62}$) (Figure 4a), such as the post-collisional hornblende gabbros from southeast Sinai [10]. Amphiboles belong to the calcic group ($\text{Ca} = 1.73\text{--}1.99$ apfu; Supplementary Table S2) and are mostly classified as magnesiohornblende with subordinate actinolite (Figure 4b). They have variable Al_2O_3 (2.11–8.65 wt.%) and low TiO_2 (0.23–1.61 wt.%) contents. Their Si and $\text{Ca} + \text{Na} + \text{K}$ (apfu) chemical characteristics suggest a magmatic origin [34]. This is supported by the $\text{Al}^{\text{IV}}/\text{Al}^{\text{VI}}$ ratios which are typical of primary igneous calcic amphiboles (Figure 4c). Their Mg# ($\text{Mg}/(\text{Mg} + \text{Fe}^{2+})$) values of 0.69 to 0.85 are similar to those of post-collisional gabbroic intrusions in the ANS [8]. Biotite is observed in a few thin sections and has a narrow compositional range (Supplementary Table S3). It is generally enriched in TiO_2 (4.31–5.11 wt.%), suggesting magmatic origin [35]. Moreover, the chemical properties indicate that it is a Mg-rich biotite of magmatic origin (Figure 4d,e). The high FeO (19.02–21.09 wt.%) and MgO (10.37–11.84 wt.%) and low MnO (0.09–0.15 wt.%) contents indicate a high temperature of crystallization [36]. The analyzed Fe-Ti oxides include ilmenite and magnetite. Ilmenite has a notably high MnO content (2.54–2.61 wt.%; Supplementary Table S4), which could be attributed to the retention of the pyrophanite (MnTiO_3) component in this phase [37].

Magnetite is chemically homogenous with the high FeO (91.21–92.45 wt.%) and low TiO_2 (0.11–0.36 wt.%) contents (Supplementary Table S4) typical of pure magnetite. Titanite has high TiO_2 (38.99–40.79 wt.%) and CaO (28.25–29.02 wt.%) with low Al_2O_3 , FeO, MnO, and MgO concentrations (Supplementary Table S5). The sulfide compositions comprise pyrite and pentlandite (Supplementary Table S6). Pyrite shows limited and high contents of S (39.40–39.66 wt.%) and Fe (57.44–58.44 wt.%) with traces of Ni and Co. Pentlandite contains high S (35.19–36.18 wt.%), Fe (28.83–31.37 wt.%), and Ni (27.15–32.46 wt.%) with low Co content (2.41–5.19 wt.%). Pyrite has clearly higher S and Fe and lower Ni and Co relative to pentlandite. Chlorite and epidote represent the main secondary minerals. The chlorite compositions display a constricted range of SiO_2 (26.83–27.11 wt.%), MgO (17.96–18.62 wt.%), Al_2O_3 (19.97–20.47 wt.%), and FeO (20.73–21.12 wt.%) contents (Supplementary Table S7). They have Si (5.56–5.62 apfu) and $\text{Fe}/(\text{Fe} + \text{Mg})$ ratios (0.39–0.40) consistent with ripidolite compositions (Figure 4f). Epidote has low FeO (8.69–9.86 wt.%) with a pistacite endmember [$\text{XPs} = \text{molar Fe}^{3+}/(\text{Fe}^{3+} + \text{Al})$ ranges from 0.19 to 0.21] (Supplementary Table S8), suggesting a secondary origin [38].

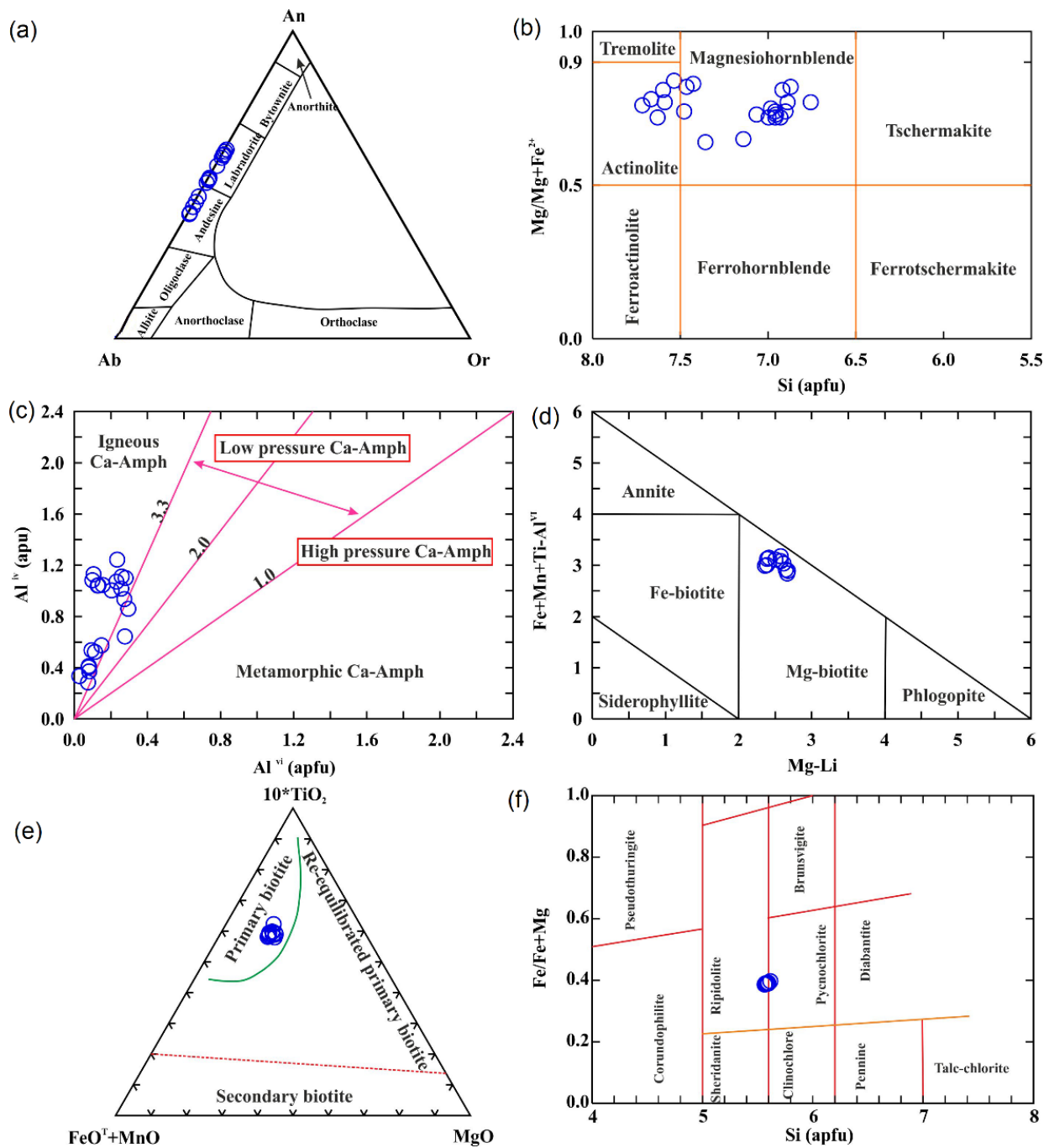


Figure 4. (a) Classification of plagioclase on Ab-Or-An ternary diagram; (b) Mg/(Mg + Fe²⁺) vs. Si classification diagram for amphiboles [39]; (c) variation of Al^{iv}/Al^{vi} ratios in Ca-amphiboles of igneous and metamorphic (low- and high-pressure) origin [40]; (d) chemical composition of biotites based on (Fe + Mn + Ti - Al^{iv}) vs. (Mg - Li) diagram [41]; (e) the (FeO^T + MnO) - (10 × TiO₂) - MgO ternary diagram of Nachit et al. [35], showing the magmatic affinity of the analyzed biotite; and (f) plot of chlorite composition in the classification diagram of Hey [42].

4.2. Bulk-Rock Geochemistry

The bulk-rock geochemical analyses of the Wadi El-Faliq hornblende gabbros are listed in Table 1. The rocks are homogeneous in composition with low LOI contents (1.15–1.63 wt.%) and display a narrow range of SiO₂ (50.17–53.13 wt.%), Al₂O₃ (17.83–19.93 wt.%), Fe₂O₃ (7.78–9.62 wt.%), MgO (4.08–6.37 wt.%), and CaO (9.32–11.29 wt.%).

They have low total alkalis (2.73–3.53 wt.%) and a sodic nature ($\text{Na}_2\text{O}/\text{K}_2\text{O} > 1$), with Mg# ($100 \times \text{Mg}/(\text{Mg} + \text{Fe}^{2+})$) ranging between 49.32 and 60.77. On the total alkalis vs. SiO_2 diagram (Figure 5a), their compositions range from gabbro to gabbroic diorite (for simplicity, hereafter, we use gabbroic rocks). They have variable compatible trace elements comprising Cr (123–218 ppm), Ni (71–124 ppm), Co (27–45 ppm), and Sc (19–29 ppm). The incompatible large ion lithophile elements (LILE) indicate significant contents (Rb = 24–42 ppm, Ba = 208–365 ppm, Sr = 472–562 ppm). Except for Zr (49–101 ppm), the samples contained low concentrations of the high field strength elements (HFSEs), particularly Th (1.5–2.3 ppm), U (0.7–1.2 ppm), Nb (2–6 ppm), Ta (0.3–1.2 ppm), and Hf (0.9–1.5 ppm).

Table 1. Bulk-rock (major, trace and REEs) geochemical data of the Wadi El-Faliq gabbro, central Eastern Desert, Egypt.

Sample	FGB-01	FGB-02	FGB-03	FGB-04	FGB-05	FGB-06	FGB-07	FGB-08	FGB-09	FGB-10	FGB-11	FGB-12	FGB-13
SiO ₂	53.13	51.99	51.07	51.18	52.23	52.07	52.81	50.17	52.39	50.17	51.41	51.29	50.27
TiO ₂	0.47	0.63	0.55	0.69	0.56	0.57	0.62	0.49	0.62	0.55	0.49	0.69	0.71
Al ₂ O ₃	17.83	18.52	18.19	19.36	18.04	18.46	18.49	18.66	19.01	19.71	18.49	18.27	19.93
Fe ₂ O ₃ ^T	7.78	8.35	9.33	8.75	8.73	9.16	8.88	7.82	8.31	8.51	9.35	9.62	8.77
MnO	0.07	0.08	0.08	0.07	0.06	0.11	0.09	0.11	0.08	0.08	0.12	0.08	0.09
MgO	5.39	4.96	5.94	5.42	6.37	5.31	4.72	6.11	4.08	4.92	4.86	4.93	5.61
CaO	10.86	10.92	10.17	10.43	9.85	9.32	9.44	11.29	10.83	10.98	10.64	10.33	10.42
Na ₂ O	2.25	2.79	2.76	2.27	2.29	2.71	2.56	2.75	2.78	2.69	2.43	2.57	2.83
K ₂ O	0.48	0.46	0.42	0.49	0.52	0.82	0.93	0.69	0.49	0.63	0.77	0.64	0.55
P ₂ O ₅	0.29	0.18	0.21	0.18	0.22	0.18	0.19	0.23	0.21	0.18	0.18	0.22	0.19
LOI	1.23	1.17	1.2	1.34	1.19	1.38	1.35	1.42	1.19	1.63	1.42	1.15	1.22
Total	99.78	100.05	99.92	100.18	100.06	100.09	100.08	99.74	99.99	100.05	100.16	99.79	100.59
Mg#	57.85	54.06	55.78	55.10	59.11	53.45	51.29	60.75	49.31	53.39	50.73	50.38	55.89
As	3.9	2.7	2.5	2.1	2.7	1.8	1.3	2.1	1.6	1.3	1.7	2.3	1.9
Ba	268	328	299	273	365	208	245	314	255	232	239	271	264
Co	32	28	31	27	35	34	36	38	41	39	45	39	34
Cr	199	138	144	208	202	218	197	191	123	157	143	182	174
Cu	33	36	27	41	53	29	46	39	24	62	34	51	49
Ga	15	16	16	15	15	21	19	17	16	18	16	15	17
Hf	1.2	1.1	0.9	1	1.5	1.1	1.5	1.3	1.2	1.4	1.2	1.1	1.3
Nb	5	5	4	2	4	5	4	4	5	6	4	5	4
Ni	95	89	105	88	111	94	79	102	76	89	124	96	71
Pb	4	2	3	3	4	6	4	5	4	7	5	5	3
Rb	24	31	38	31	29	40	37	36	35	34	39	33	42
Sc	21	27	19	28	24	25	26	28	27	29	26	27	24
Sr	531	496	556	478	512	562	551	559	472	516	548	493	477
Ta	0.5	0.4	1.2	0.6	0.8	0.4	0.5	0.4	0.3	0.6	0.5	0.4	0.7
Th	2.1	1.7	1.8	1.5	1.9	1.8	2.2	2.1	2	2.2	2.3	1.9	1.7
U	0.9	1.2	0.8	0.9	1.2	0.7	1.2	0.9	1.1	1.3	0.9	1.2	0.8
V	182	194	197	193	185	218	169	184	178	201	193	159	145
Y	8	10	9	8	11	12	14	9	13	11	9	12	10
Zn	66	64	61	58	59	63	71	65	69	68	71	63	72
Zr	82	77	76	81	83	101	78	65	98	67	49	93	69
La	12.21	-	17.51	-	14.84	12.71	-	18.32	13.09	-	-	18.12	14.95
Ce	27.30	-	29.14	-	23.04	28.28	-	21.12	24.47	-	-	31.69	27.95
Pr	2.91	-	3.04	-	2.85	3.15	-	2.91	2.78	-	-	3.12	3.01
Nd	14.37	-	14.45	-	13.25	13.69	-	12.97	14.65	-	-	13.82	12.66
Sm	3.14	-	3.28	-	3.78	2.98	-	3.09	2.99	-	-	3.48	3.72
Eu	1.07	-	0.97	-	0.95	1.05	-	1.06	1.11	-	-	1.03	0.99
Gd	3.22	-	3.86	-	3.45	3.41	-	3.08	2.78	-	-	3.09	4.02
Tb	0.55	-	0.62	-	0.49	0.52	-	0.46	0.57	-	-	0.43	0.53
Dy	2.56	-	2.59	-	2.81	2.49	-	2.61	3.01	-	-	2.81	3.11
Ho	0.69	-	0.55	-	0.58	0.65	-	0.67	0.61	-	-	0.63	0.78
Er	1.59	-	1.67	-	1.46	1.57	-	1.44	1.38	-	-	1.46	1.61
Tm	0.22	-	0.24	-	0.31	0.27	-	0.29	0.23	-	-	0.24	0.31
Yb	1.57	-	1.48	-	1.51	1.68	-	1.53	1.42	-	-	1.55	1.33
Lu	0.21	-	0.23	-	0.2	0.23	-	0.24	0.19	-	-	0.23	0.21

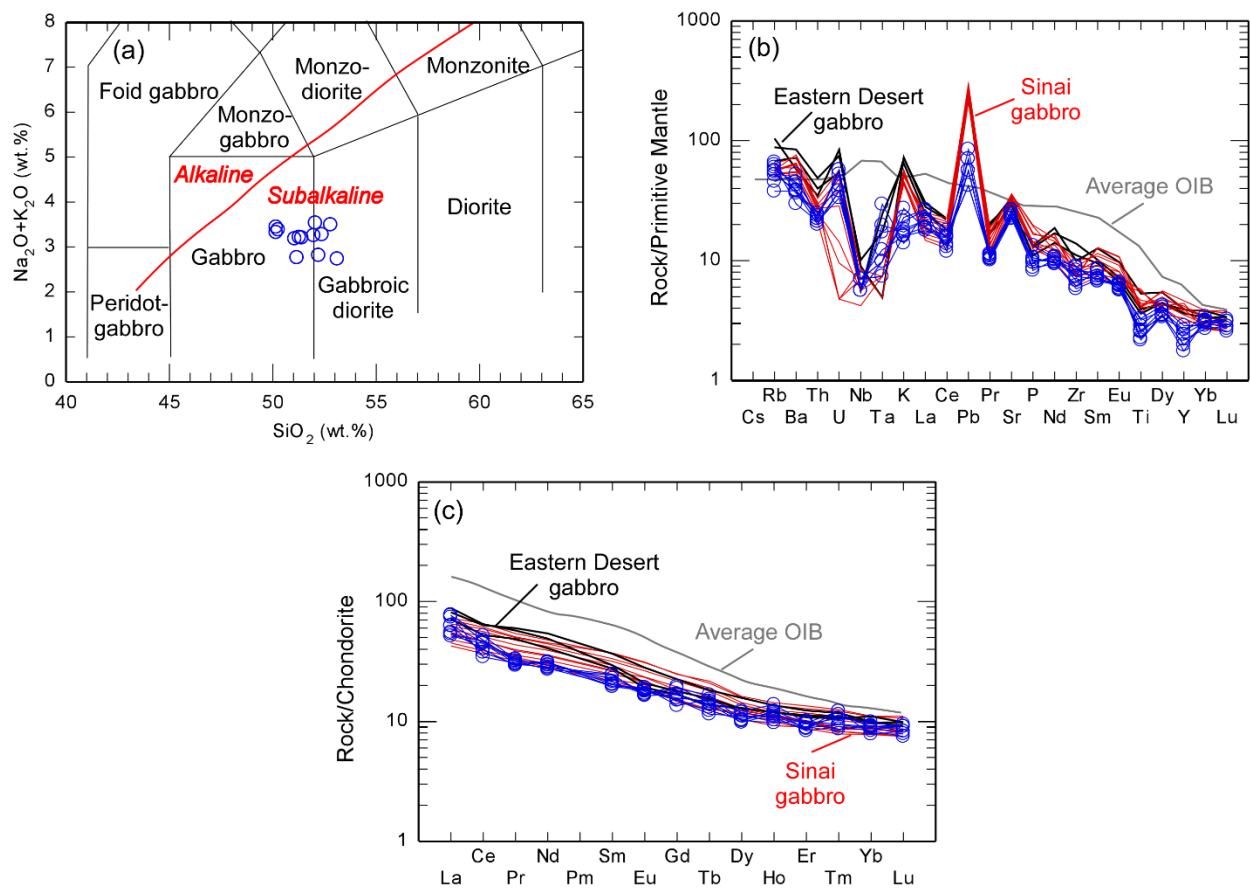


Figure 5. (a) Total alkalis vs. SiO₂ [43]. The red line separates alkaline and subalkaline compositions adopted from Irvine and Baragar [44]; (b) primitive mantle-normalized trace element patterns; and (c) chondrite-normalized REE patterns. Normalization values and average OIB are from Sun and McDonough [45]. Post-collisional gabbros from the Eastern Desert and southeast Sinai in the ANS were used for comparison [10,46].

The primitive mantle-normalized spider diagram (Figure 5b) shows that the studied gabbroic rocks are enriched in Pb and depleted in HFSE (Th, Nb, Ti, and Y). The characteristic positive-Pb anomalies and HFSE depletion are comparable to those of post-collisional gabbros from the Eastern Desert and southeast Sinai [10,46] (Figure 5b). The trace element patterns are distinctive compared to average Ocean Island Basalt (OIB) with variable anomalies (Figure 5b). The chondrite-normalized REE patterns (Figure 5c) show relatively steep patterns enriched in LREEs compared to HREEs without Ce anomalies. The range of Eu anomalies ($\text{Eu}/\text{Eu}^* = 0.78\text{--}1.18$) are comparable to those of the Eastern Desert and Sinai post-collisional gabbros [10,46]. Compared to average OIB, they are REE-depleted, particularly in LREEs, and have somewhat similar HREEs (Figure 5c). The REE patterns are identical to post-collisional gabbros from the Eastern Desert and southeast Sinai (Figure 5c). The trace and REE patterns are generally comparable (Figure 5b,c). They show Zr/Hf ratios (40.8–91.8) higher than the chondritic value (34.3 ± 0.3 ; [47]), resembling those observed in oceanic and continental basalts [11,12,48].

5. Discussion

5.1. Post-Magmatic Alteration and Crustal Contamination

The low LOI contents and the absence of Ce anomalies (Figure 5c) indicate insignificant post-magmatic alteration, consistent with petrographic investigation. Moreover, their alkali contents are typical of unaltered gabbros (Figure 6a). The sub-chondritic Nb/Ta (3.33–16.67) ratios further confirm this inference and reflect the mantle composition [49]. The low

Th/La ratios (0.10–0.17) and negative Th anomalies (Figure 5b) exclude contamination with crustal materials [50]. Moreover, the low Th/Ce (0.06–0.10) and Th/Nb (0.34–0.75) ratios rule out crustal contamination processes from gabbroic magma genesis [51]. The average concentrations of Ba (274 ppm) and Sr (519 ppm) are higher than those of the continental crust (Ba = 259 ppm, Sr = 348 ppm; [52]). Moreover, they possess low Lu/Yb (0.13–0.16) ratios identical to mantle-derived magmas and lower than continental crust, consistent with derivation from a mantle source lacking contamination with continental crust materials [45,52]. As a result, their bulk-rock data reveal a primary magmatic signature and reflect mantle source characteristics.

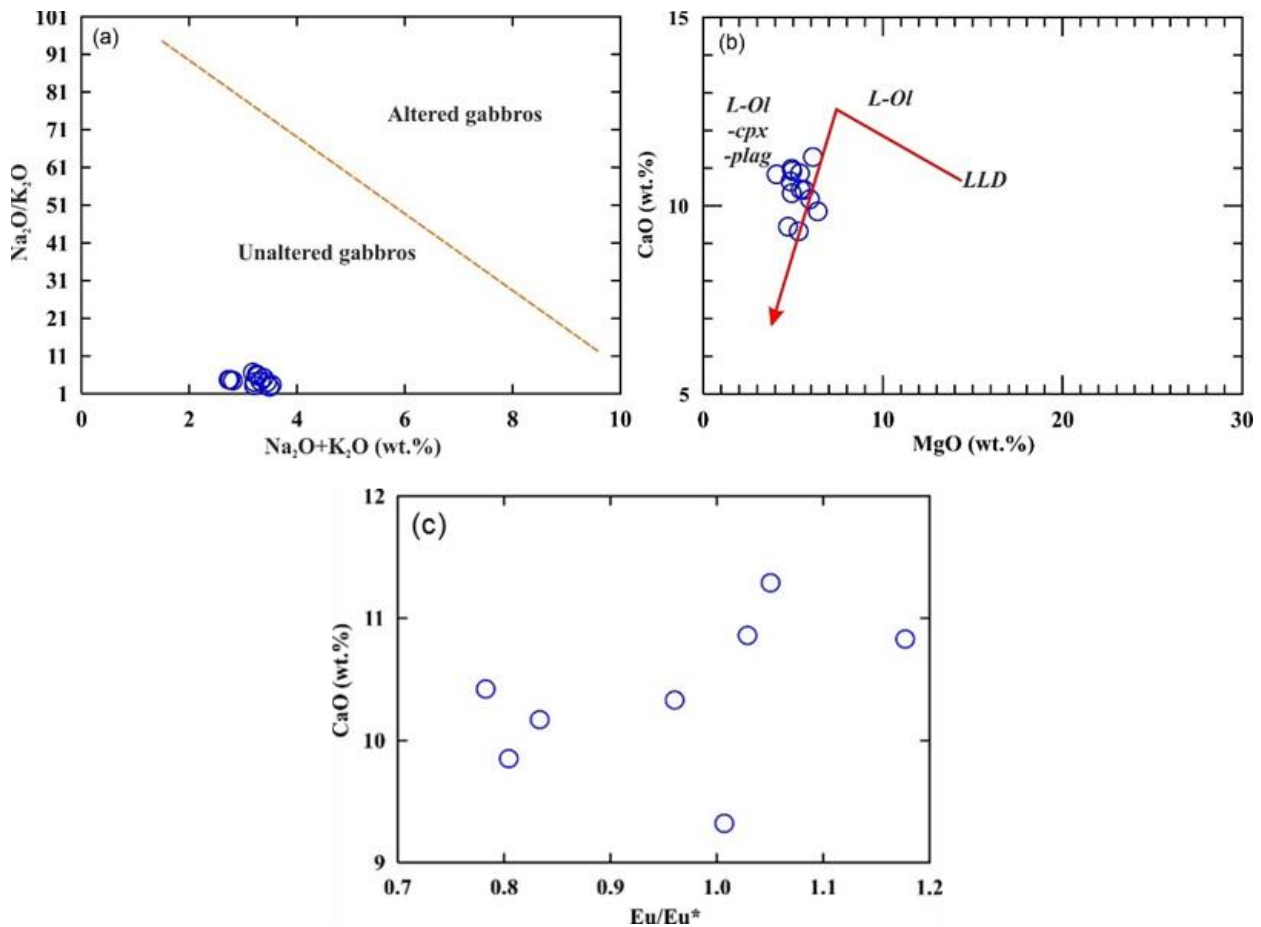


Figure 6. (a) Plot of Na₂O + K₂O vs. Na₂O/K₂O [53], showing the unaltered nature of the rocks; and (b) plot of MgO vs. CaO. The red broken arrow is the typical liquid line of descent (LLD) for primary magmas that crystallize gabbro in the crust [54]; and (c) plot of Eu/Eu* vs. CaO.

5.2. Crystal Fractionation

The primary mafic magmas equilibrated with upper mantle mineralogy show high Mg# values (>70), compatible trace elements (Ni > 400–500 ppm, Cr > 1000 ppm) and low SiO₂ contents (<50 wt.%) [55]. So, the low Mg# values and compatible trace element contents of the studied rocks indicate that they do not represent primary magma and have experienced varying degrees of crystal fractionation before emplacement. The relatively wide range of Mg# values as well as the Cr, Ni, and Sc contents reflect variable degrees of olivine and clinopyroxene fractionation. Indeed, the range of CaO and MgO contents in the studied rocks follows the typical liquid line of descent (LLD) for primary magmas that crystallize gabbros in the crust (Figure 6b). In Figure 6b, the noticed CaO drop often arises at a range of MgO content below ~7–10 wt.%, which is consistent with the fractionation of olivine, clinopyroxene, and plagioclase from their primary magmas [54]. This drop in

CaO characterizes the differentiated mafic magmas that crystallize gabbros in the crust [54]. The studied rocks follow the LLD trend, which indicates fractionation of olivine, pyroxene, and plagioclase and argues for the evolved nature of the studied rocks. Although the presence of Eu anomalies ($\text{Eu}/\text{Eu}^* = 0.78\text{--}1.18$) may suggest plagioclase fractionation, the lack of correlation between the CaO and Eu/Eu^* (Figure 6c) excludes a role of plagioclase fractionation. Accordingly, olivine and pyroxene represent the main fractionating phases.

5.3. Nature of the Mantle Source and Melting Conditions

Mantle-derived magma has low Lu/Yb ratios, which is the case for the studied gabbroic rocks ($\text{Lu}/\text{Yb} = 0.13\text{--}0.16$; [45]). Moreover, they show identical chondrite-normalized REE patterns consistent with derivation from a common mantle source. The sub-chondritic Nb/U (2.22–7.14) and Nb/Ta (3.3–16.67) ratios reveal mantle source depletion by a former melting extraction event [56]. Zr and Nb concentrations can reveal mantle source enrichment or depletion [57]. The Zr versus Nb relationship confirms the generation of gabbroic magma from a depleted mantle source (Figure 7a).

Oceanic basalts show relatively high and uniform Nb/U ratios [58]. In contrast, several continental flood basalts show low Nb/U and Nb/La ratios [59]. Arndt and Christensen [60] suggest that the negative Nb anomalies observed in several continental flood basalts could not be generated directly from the melting of the lithospheric mantle source. They showed that the Nb fractionation likely arises from the melt-rock reaction process. This process occurs during asthenospheric melt ascent through the lithosphere mantle due to the different reaction rates of minerals in metasomatized peridotite [59,60]. The low Nb/U (2.22–7.14) and Nb/La (0.22–0.41) ratios of the studied gabbroic rocks along with the negative Nb anomalies likely suggest the contribution of such a fractionation process in their genesis. Therefore, the melt-rock reactions during the ascent of the asthenospheric melt through the lithospheric mantle could explain the origin of the studied gabbroic rocks [59]. Furthermore, the origin of the post-collisional gabbros in the Arabian Shield was attributed to this process [8].

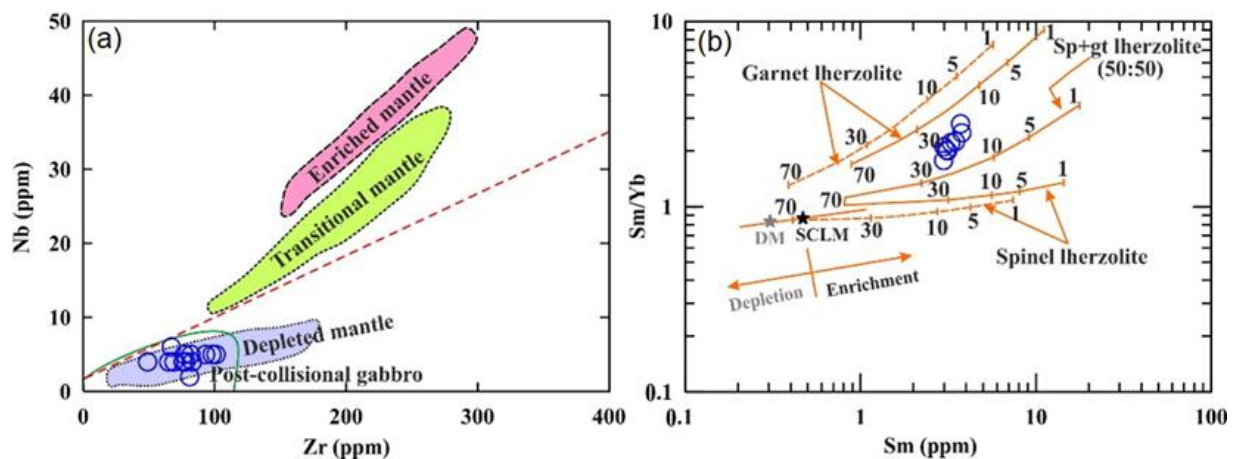


Figure 7. (a) Zr–Nb diagram [57]. Post-collisional gabbro field is used for comparison [8,10]; and (b) Sm/Yb vs. Sm diagram [61], showing melt curves for different starting materials (garnet lherzolite, spinel + garnet lherzolite, and spinel lherzolite) based on the non-batch melting equations of Shaw [62]. The dashed and solid curves represent the melting trends for depleted mantle (DM, $\text{Sm} = 0.3$ ppm and $\text{Sm}/\text{Yb} = 0.86$; [63]) and enriched subcontinental lithospheric mantle (SCLM, $\text{Sm} = 0.6$ ppm and $\text{Sm}/\text{Yb} = 0.96$; [64]), respectively. Partition coefficients are from McKenzie and O’Nions [63]. The numbers refer to the degrees of partial melting.

The high $(\text{Gd}/\text{Yb})_{\text{N}}$ ratios (1.62–2.5) of the studied rocks reveal residual garnet in the source region during melting [65]. The asthenosphere mantle source is predominantly garnet peridotite; however, anhydrous garnet peridotite is not a proper mantle source for the studied gabbroic rocks due to their super-chondritic Zr/Hf ratios. These ratios cannot

be generated by the melting of a dry garnet peridotite source but require a volatile contribution [66], because peridotite shows analogous Zr and Hf partitioning coefficients [67]. This inference is supported by presence of hydrous minerals of primary igneous origin such as amphibole and biotite, which reveal crystallization from hydrous magma. Amphibole crystallization requires magma with a high-water content (>3 wt.%; [68]. The very low Nb/Th (<8) and variable Zr/Nb (11–41) ratios also indicate a hydrated mantle source [69].

The REEs, particularly HREEs in mafic magmas, are commonly used to constrain the mantle-melting depths [70,71]. This is possibly due to their dramatic changes in partitioning during partial melting of spinel peridotites against garnet peridotites. Garnet shows a strong preference for HREE, and thus melts in equilibrium with garnet having high $(\text{Tb}/\text{Yb})_N$ and $(\text{Dy}/\text{Yb})_N$ ratios [70,71]. Due to garnet stability in mantle peridotite at higher pressures compared to spinel, the REEs, particularly the HREEs, can be used as a kind of geobarometer [72]. Blundy et al. [70] suggested that partial melts produced from a spinel-peridotite source show nearly flat chondrite-normalized HREE patterns, i.e., $(\text{Dy}/\text{Yb})_N$ ratios ≤ 1.06 , whereas those generated from a garnet-peridotite source have $(\text{Dy}/\text{Yb})_N$ ratios > 1.06 . The studied gabbroic rocks display a wide range of $(\text{Dy}/\text{Yb})_N$ ratios (0.99–1.57), which possibly indicate a mixing between partial melts of both spinel and garnet peridotites. Garnet signatures can be estimated from the $(\text{Tb}/\text{Yb})_N$ ratios, where higher ratios (>1.8) indicate higher pressures of partial melting in the garnet stability field [71]. The studied gabbroic rocks also show a wide range of $(\text{Tb}/\text{Yb})_N$ ratios (1.27–1.9), suggesting that the fractionation of HREEs cannot be explained by the melting of a single mantle source but requires the mixing of melts from both the spinel- and garnet-bearing peridotite-mantle sources [71]. Thus, the melting probably occurs at depths between the spinel and garnet stability fields, indicating a moderate depth of melting (i.e., 60–80 km). Since Yb is strongly compatible with garnet, the Sm/Yb ratio is garnet-dependent and is used to constrain the mineralogy of the mantle source in mafic magmas [64]. The Sm/Yb versus Sm diagram (Figure 7b) shows that all rock samples are plotted between the garnet- and spinel + garnet-lherzolite melting curves, further supporting the presence of garnet and spinel in the mineralogy of the mantle source. It is obvious that the studied samples displaced from the spinel + garnet-lherzolite (50:50) melting curve to the garnet-lherzolite melting curve, suggesting more garnet than spinel (Figure 7b). According to Figure 7b, the studied gabbroic rocks may be crystallized from melts produced by about 10–30% degrees of partial melting.

5.4. Geotectonic Setting and Magmatic Affinity

The field relationships show that the gabbroic rocks are intruded by the post-collisional alkali-feldspar granites (Figure 2) and are undeformed and unmetamorphosed. The geochemical characteristics also support their unmetamorphosed nature (Figure 6a). Moreover, the gabbroic and granitic intrusions show a NW–SE trend, like that of the NFS, which likely suggests a relation to the extension associated with the NFS at the end of the Pan-African orogeny. The presence of primary amphibole and biotite in the studied rocks reflects the hydrous nature of the parental mafic magma. The rocks belong to the sub-alkaline suite and exhibit tholeiitic affinity (Figures 5a and 8a). They show high La/Nb ratios (2.4–4.6) reflecting a subduction-like signature [69]. The negative-Nb and positive-Pb anomalies and the high Ba/Nb (38.7–136.5) and La/Sm_N (2.51–3.83) ratios also confirm the subduction-like characteristics [56,73,74]. They have Nb/Th and La/Nb ratios comparable to those of arc-like gabbroic rocks (Figure 8b). Additionally, they are plotted in the tholeiite field of arc and within-plate rocks (Figure 8c), supporting both the arc-like and the rift-related signatures. The subduction- and arc-like signatures, possibly resulting from the melting of a mantle source, metasomatized during the former subduction phase in the ANS [8,10,12]. A subduction-like signature in a post-collisional intrusion is likely due to the inheritance of geochemical tendencies from the former subduction phase in the ANS [8,10]. Moreover, the Pb enrichment and the HFSE depletion (Figure 5b) along with the REE patterns (Figure 5c) all resemble other post-collisional gabbros in the

ANS [8,10,15,28,46]. The $\text{TiO}_2\text{-Y}/20\text{-K}_2\text{O}$ ternary diagram indicates affinity to intracontinental rift gabbros (Figure 8d). Moreover, they overlap the field of the post-collisional gabbros from ANS (Figures 7a and 8a,b). These inferences suggest that they were probably derived from hydrous tholeiitic magma emplaced in a post-collisional setting during an extensional phase at the end of the Pan-African orogeny.

5.5. Geodynamic Setting

The Neoproterozoic evolution of Egypt involves three main tectono-metamorphic events. Ophiolite obduction and island-arc terrane accretion represent the first event (820–720 Ma) [75]. The collisional stage is the second event (620–650 Ma); during this period, the accreted juvenile terranes were attached to the East Saharan Craton [76]. The post-collisional stage represents the third event during which widespread calc-alkaline (630–590 Ma) and alkaline (610–580 Ma) magmatism intruded the northern part of the ANS, pointing to their coeval generation between 610 and 590 Ma [77]. This magmatism is markedly distinct from the arc-related (collisional) one that was produced via the consumption of the Mozambique oceanic crust and the accretion of West and East Gondwana. The studied gabbroic rocks show geochemical characteristics consistent with subduction- and arc-like magmas (Figure 8b,c). However, their unmetamorphosed and undeformed nature along with their field relationships indicate that the studied gabbroic intrusion is post-orogenic and post-dates the main collisional stage, supporting its emplacement after subduction termination. Moreover, they show geochemical characteristics consistent with post-collisional gabbroic intrusions (Figure 5b,c, Figures 7a and 8a,b). These features distinguish them from the early phases of subduction- and arc-related gabbros, which are both metamorphosed and deformed [10,78]. The subduction-like geochemical signature of the studied rocks was probably inherited from the previous subduction event in the ANS [10,78].

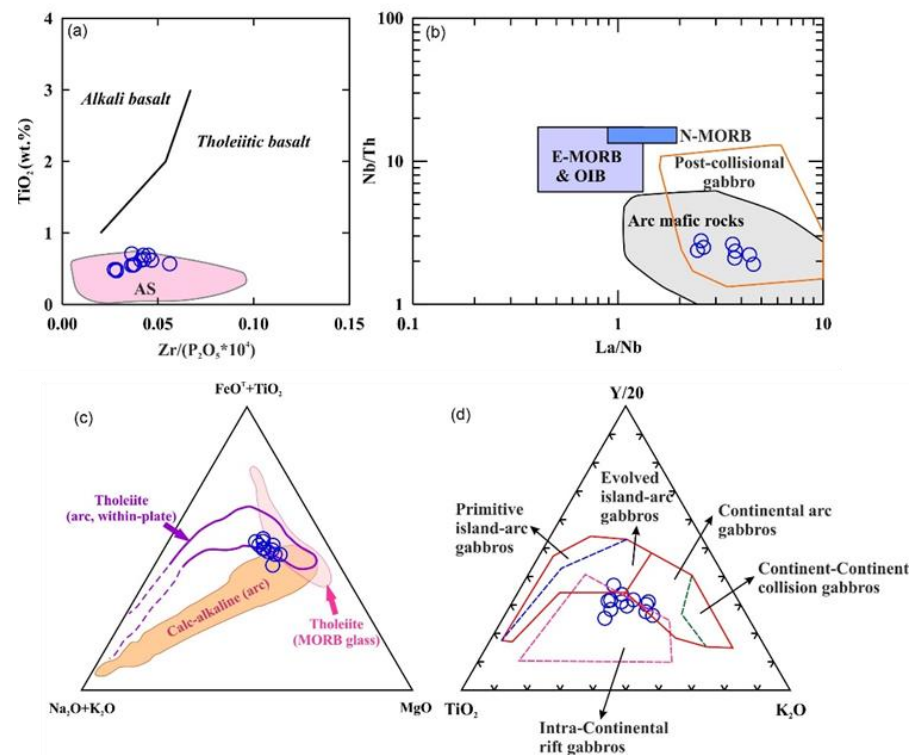


Figure 8. (a) $\text{Zr}/(\text{P}_2\text{O}_5 \times 104)$ vs. TiO_2 diagram [79]. AS field represents post-collisional gabbros from Arabian Shield [8]; (b) La/Nb vs. Nb/Th diagram [80]. Post-collisional gabbros field is from Khalil et al. [10] and Ali and Alshammari [8]; (c) discrimination diagram for calc-alkaline and tholeiite igneous rocks [44]; and (d) $\text{TiO}_2\text{-Y}/20\text{-K}_2\text{O}$ triangular diagram discriminating between arc and continental gabbros [81].

Post-collisional magmatism forms as a result of lithospheric extension and asthenospheric mantle upwelling in the final stage of the orogenic process [82]. In the ANS, post-collisional magmatism has been attributed to a lithospheric delamination mechanism [7,83]. Lithospheric delamination permits the rapid rising of the asthenosphere mantle and melting due to the adiabatic release of pressure. Faults and shear zones formed during post-orogenic crustal extension assisted in this process [84]. The prevalence of extensional structures in the Eastern Desert of Egypt, such as strike-slip faults and shear zones of the NFS, metamorphic core complexes, and dyke swarms, supports this mechanism [84]. Therefore, younger post-collisional gabbroic intrusions in the ANS, including the studied rocks, are related to the extension associated with the orogenic collapse [27,85].

6. Conclusions

The Wadi El-Faliq gabbroic intrusion, a part of the Precambrian basement rocks of the central Eastern Desert of Egypt, is a fresh, undeformed elliptical body, elongated in a NW–SE trend, tracking the major sinistral strike-slip faults of the NFS. The mineralogical and geochemical characteristics indicate its derivation from hydrous tholeiitic mafic magmas with arc-like geochemical signatures similar to the post-collisional gabbroic intrusions in Saudi Arabia. Despite the arc-like signatures, its fresh and undeformed nature, along with the field relationships, suggests that the studied gabbroic intrusion post-dates the main collisional stage and supports its intrusion after subduction termination during the post-collisional stage. Accordingly, the arc-like fingerprints were probably inherited from the earlier subduction phase of the ANS. In fact, the elevated $(La/Sm)_N$ and negative-Nb and positive-Pb anomalies indicate the influence of subduction components. The Najd faults and shear zones created during the post-orogenic crustal extension associated with orogenic collapse possibly caused lithospheric delamination, which in turn could have produced rapid upwelling and melting of the asthenosphere mantle. The melt-rock reaction process, where asthenospheric melts interacted during ascent with the lithosphere mantle rocks, likely played an important role in the gabbroic rock genesis. The HREE fractionation might indicate the mixing of melts from both spinel- and garnet-bearing peridotites. Based on the available data, we propose that the emplacement of the Wadi El-Faliq gabbroic intrusion is perhaps related to the stretching and thinning of the lithosphere during the extensional tectonics following the Pan-African orogeny.

Supplementary Materials: The following supporting information can be downloaded at: <https://www.mdpi.com/article/10.3390/min13010010/s1>, Table S1: Electron microprobe analyses of plagioclase from the Wadi El-Faliq gabbros; Table S2: Electron microprobe analyses of amphibole from the Wadi El-Faliq gabbro; Table S3: Electron microprobe analyses of biotite from the Wadi El-Faliq gabbro; Table S4: Electron microprobe analyses of Fe-Ti oxides from the Wadi El-Faliq gabbro; Table S5: Electron microprobe analyses of titanite from the Wadi El-Faliq gabbro; Table S6: Electron microprobe analyses of pyrite and pentlandite from the Wadi El-Faliq gabbro; Table S7: Electron microprobe analyses of chlorite from the the Wadi El-Faliq gabbro; Table S8: Electron microprobe analyses of epidote from the Wadi El-Faliq gabbro; Document S1: Analytical methods.

Author Contributions: Conceptualization, S.A., M.I.S. and M.S.; methodology, R.A.; software, M.S.; validation, S.A., M.S. and M.I.S.; formal analysis, R.A. and C.A.H.; investigation, M.S.; resources, S.A.; data curation, R.A.; writing—original draft preparation, S.A.; writing—review and editing, M.S.; visualization, M.S.; supervision, S.A. All authors have read and agreed to the published version of the manuscript.

Funding: This research received no external funding.

Data Availability Statement: Not applicable.

Acknowledgments: The authors would like to thank Theodoros Ntaflos and Franz Kiraly for assistance with the electron microprobe and the staff members and technicians of the Department of Lithospheric Research, University of Vienna. Mabrouk Sami would like to thank the Ministry of Higher Education of Egypt for supporting his research stay at the University of Vienna (Austria) as a

postdoctoral fellow. We thank the two anonymous reviewers who provided insightful comments that enhanced this manuscript.

Conflicts of Interest: The authors declare no conflict of interest.

References

1. Sami, M.; Ntaflos, T.; Farahat, E.S.; Mohamed, H.A.; Ahmed, A.F.; Hauzenberger, C. Mineralogical, geochemical and Sr-Nd isotopes characteristics of fluorite-bearing granites in the Northern Arabian-Nubian Shield, Egypt: Constraints on petrogenesis and evolution of their associated rare metal mineralization. *Ore Geology Reviews* **2017**, *88*, 1–22. [\[CrossRef\]](#)
2. Patchett, P.J.; Chase, C.G. Role of transform continental margins in major crustal growth episodes. *Geology* **2002**, *30*, 39. [\[CrossRef\]](#)
3. Stoesser, D.B.; Frost, C.D. Nd, Pb, Sr, and O isotopic characterization of Saudi Arabian Shield terranes. *Chem. Geol.* **2006**, *226*, 163–188. [\[CrossRef\]](#)
4. Adam, M.M.A.; Lv, X.; Fathy, D.; Abdel Rahman, A.R.A.; Ali, A.A.; Mohammed, A.S.; Farahat, E.S.; Sami, M. Petrogenesis and tectonic implications of Tonian island arc volcanic rocks from the Gabgaba Terrane in the Arabian-Nubian Shield (NE Sudan). *J. Asian Earth Sci.* **2022**, *223*, 105006. [\[CrossRef\]](#)
5. Stern, R.J. Crustal evolution in the East African Orogen: A neodymium isotopic perspective. *J. Afr. Earth Sci.* **2002**, *34*, 109–117. [\[CrossRef\]](#)
6. Eyal, M.; Litvinovsky, B.; Jahn, B.M.; Zanvilevich, A.; Katzir, Y. Origin and evolution of post-collisional magmatism: Coeval Neoproterozoic calc-alkaline and alkaline suites of the Sinai Peninsula. *Chem. Geol.* **2010**, *269*, 153–179. [\[CrossRef\]](#)
7. Farahat, E.S.; Zaki, R.; Hauzenberger, C.; Sami, M. Neoproterozoic calc-alkaline peraluminous granitoids of the Deleihimmi pluton, Central Eastern Desert, Egypt: Implications for transition from late- to post-collisional tectonomagmatic evolution in the northern Arabian-Nubian Shield. *Geol. J.* **2011**, *46*, 544–560. [\[CrossRef\]](#)
8. Ali, S.; Alshammari, A.S. Genesis of gabbroic intrusions in the Arabian Shield, Saudi Arabia: Mineralogical, geochemical and tectonic fingerprints of the Neoproterozoic arc magmatism. *Geol. Mag.* **2021**, *158*, 1639–1656. [\[CrossRef\]](#)
9. Sami, M.; El Monsef, M.A.; Abart, R.; Toksoy-Köksal, F.; Abdelfadil, K.M. Unraveling the Genesis of Highly Fractionated Rare-Metal Granites in the Nubian Shield via the Rare-Earth Elements Tetrad Effect, Sr–Nd Isotope Systematics, and Mineral Chemistry. *ACS Earth Space Chem.* **2022**, *6*, 2368–2384. [\[CrossRef\]](#)
10. Khalil, A.E.S.; Obeid, M.A.; Azer, M.K. Late Neoproterozoic post-collisional mafic magmatism in the Arabian–Nubian Shield: A case study from Wadi El-Mahash gabbroic intrusion in southeast Sinai, Egypt. *J. Afr. Earth Sci.* **2015**, *105*, 29–46. [\[CrossRef\]](#)
11. Farahat, E.S.; Ali, S.; Hauzenberger, C. Red Sea rift-related Quseir basalts, central Eastern Desert, Egypt: Petrogenesis and tectonic processes. *Bull. Volcanol.* **2017**, *79*, 9. [\[CrossRef\]](#)
12. Farahat, E.S.; Ali, S.; Liu, Y. Origin and geotectonic evolution of Mir Tertiary basaltic andesite dykes, Western Desert, Egypt: Constraints from mineral and bulk-rock chemistry. *Geol. J.* **2019**, *54*, 2274–2287. [\[CrossRef\]](#)
13. Ali, S.; Ntaflos, T.; Sami, M. Geochemistry of Khor Um-Safi ophiolitic serpentinites, central Eastern desert, Egypt: Implications for neoproterozoic arc-basin system in the Arabian-Nubian shield. *Geochemistry* **2021**, *81*, 125690. [\[CrossRef\]](#)
14. Mogahed, M.M. Petrogenesis of Zeiatit gabbroic rocks in the Southern Eastern Desert of Egypt: Discrimination of arc-related Neoproterozoic gabbros. *J. Afr. Earth Sci.* **2019**, *150*, 239–263. [\[CrossRef\]](#)
15. Abdelfadil, K.M.; Saleh, G.M.; Putiš, M.; Sami, M. Mantle source characteristics of the late Neoproterozoic post-collisional gabbroic intrusion of Wadi Abu Hadieda, north Arabian-Nubian Shield, Egypt. *J. Afr. Earth Sci.* **2022**, *194*, 104607. [\[CrossRef\]](#)
16. Azer, M.K.; El-Gharbawy, R.I. The Neoproterozoic layered mafic–ultramafic intrusion of Gabal Imleih, south Sinai, Egypt: Implications of post-collisional magmatism in the north Arabian–Nubian Shield. *J. Afr. Earth Sci.* **2011**, *60*, 253–272. [\[CrossRef\]](#)
17. Obeid, M.A.; Khalil, A.E.S.; Azer, M.K. Mineralogy, geochemistry, and geotectonic significance of the Neoproterozoic ophiolite of Wadi Arais area, south Eastern Desert, Egypt. *Int. Geol. Rev.* **2015**, *58*, 687–702. [\[CrossRef\]](#)
18. Stern, R.J.; Ali, K.; Asimow, P.D.; Azer, M.K.; Leybourne, M.I.; Mubarak, H.S.; Ren, M.; Romer, R.L.; Whitehouse, M.J. The Atud gabbro–diorite complex: Glimpse of the Cryogenian mixing, assimilation, storage and homogenization zone beneath the Eastern Desert of Egypt. *J. Geol. Soc.* **2020**, *177*, 965–980. [\[CrossRef\]](#)
19. Abu Anbar, M.M. Petrogenesis of the Nesryin gabbroic intrusion in SW Sinai, Egypt: New contributions from mineralogy, geochemistry, Nd and Sr isotopes. *Mineral. Petrol.* **2009**, *95*, 87–103. [\[CrossRef\]](#)
20. Mahdy, N.M.; Ntaflos, T.; Pease, V.; Sami, M.; Slobodník, M.; Abu Steet, A.A.; Abdelfadil, K.M.; Fathy, D. Combined zircon U–Pb dating and chemical Th–U–total Pb chronology of monazite and thorite, Abu Diab A-type granite, Central Eastern Desert of Egypt: Constraints on the timing and magmatic-hydrothermal evolution of rare metal granitic magmatism in the Arabian Nubian Shield. *Geochemistry* **2020**, *80*, 125669. [\[CrossRef\]](#)
21. Genna, A.; Nehlig, P.; Le Goff, E.; Guerrot, C.; Shanti, M. Proterozoic tectonism of the Arabian Shield. *Precambrian Res.* **2002**, *117*, 21–40. [\[CrossRef\]](#)
22. Johnson, P.R.; Woldehaimanot, B. Development of the Arabian-Nubian Shield: Perspectives on accretion and deformation in the northern East African Orogen and the assembly of Gondwana. *Geol. Soc. Lond. Spec. Publ.* **2022**, *206*, 289–325. [\[CrossRef\]](#)
23. Fritz, H.; Wallbrecher, E.; Khudeir, A.; El Ela, F.A.; Dallmeyer, D. Formation of Neoproterozoic metamorphic complex during oblique convergence (Eastern Desert, Egypt). *J. Afr. Earth Sci.* **1996**, *23*, 311–329. [\[CrossRef\]](#)

24. Abu-Alam, T.S.; StÜWe, K. Exhumation during oblique transpression: The Feiran-Solaf region, Egypt. *J. Metamorph. Geol.* **2009**, *27*, 439–459. [[CrossRef](#)]
25. Sami, M.; Ntaflos, T.; Mohamed, H.A.; Farahat, E.S.; Hauzenberger, C.; Mahdy, N.M.; Abdelfadil, K.M.; Fathy, D. Origin and Petrogenetic Implications of Spessartine Garnet in Highly-Fractionated Granite from the Central Eastern Desert of Egypt. *Acta Geol. Sin.—Engl. Ed.* **2020**, *94*, 763–776. [[CrossRef](#)]
26. Abdel-Rahman, A.-F.M. Mineralogy of the Neoproterozoic epidote-bearing TTG suite, Mons Claudianus batholith (Egypt) and implications for synorogenic magmatism. *Miner. Mag* **2018**, *80*, 1291–1314. [[CrossRef](#)]
27. Johnson, P.R.; Andresen, A.; Collins, A.S.; Fowler, A.R.; Fritz, H.; Ghebreab, W.; Kusky, T.; Stern, R.J. Late Cryogenian–Ediacaran history of the Arabian–Nubian Shield: A review of depositional, plutonic, structural, and tectonic events in the closing stages of the northern East African Orogen. *J. Afr. Earth Sci.* **2011**, *61*, 167–232. [[CrossRef](#)]
28. Surour, A.A.; Ahmed, A.H.; Harbi, H.M. Mineral chemistry as a tool for understanding the petrogenesis of Cryogenian (arc-related)–Ediacaran (post-collisional) gabbros in the western Arabian Shield of Saudi Arabia. *Int. J. Earth Sci.* **2016**, *106*, 1597–1617. [[CrossRef](#)]
29. Abdel-Karim, A.-A.; Azer, M.; Sami, M. Petrogenesis and tectonic implications of the Maladob ring complex in the South Eastern Desert, Egypt: New insights from mineral chemistry and whole-rock geochemistry. *Int. J. Earth Sci.* **2020**, *110*, 53–80. [[CrossRef](#)]
30. Stern, R.J. Arc assembly and continental collision in the neoproterozoic east african orogen: Implications for the Consolidation of Gondwanaland. *Annu. Rev. Earth Planet. Sci.* **1994**, *22*, 319–351. [[CrossRef](#)]
31. Azer, M.K.; Abdelfadil, K.M.; Asimow, P.D.; Khalil, A.E.; Bozkurt, E. Tracking the transition from subduction-related to post-collisional magmatism in the north Arabian–Nubian Shield: A case study from the Homrit Waggat area of the Eastern Desert of Egypt. *Geol. J.* **2019**, *55*, 4426–4452. [[CrossRef](#)]
32. Hassanen, M.A. Post-collision, A-type granites of Homrit Waggat complex, Egypt: Petrological and geochemical constraints on its origin. *Precambrian Res.* **1997**, *82*, 211–236. [[CrossRef](#)]
33. Moghazi, A.; Mohamed, F.; Kanisawa, S. Geochemical and petrological evidence of calc-alkaline and A-type magmatism in the Homrit Waggat and El-Yatima areas of eastern Egypt. *J. Afr. Earth Sci.* **1999**, *29*, 535–549. [[CrossRef](#)]
34. Giret, A.; Bonin, B.; Leger, J.-M. Amphibole compositional trends in oversaturated and undersaturated alkaline plutonic ring-composition. *Can. Mineral.* **1980**, *18*, 481–495.
35. Nachit, H.; Ibhi, A.; Abia, E.H.; Ben Ohoud, M. Discrimination between primary magmatic biotites, reequilibrated biotites and neofomed biotites. *Comptes Rendus Geosci.* **2005**, *337*, 1415–1420. [[CrossRef](#)]
36. Henry, D.J.; Guidotti, C.V.; Thomson, J.A. The Ti-saturation surface for low-to-medium pressure metapelitic biotites: Implications for geothermometry and Ti-substitution mechanisms. *Am. Mineral.* **2005**, *90*, 316–328. [[CrossRef](#)]
37. Sasaki, K.; Nakashima, K.; Kanisawa, S. Pyrophanite and high Mn ilmenite discovered in the Cretaceous Tono pluton, NE Japan. *Neues Jahrb. Mineral.—Mon.* **2003**, *2003*, 302–320. [[CrossRef](#)]
38. Johnston, A.D.; Wyllie, P.J. Constraints on the origin of Archean trondhjemites based on phase relationships of Nuk gneiss with H₂O at 15 kbar. *Contrib. Mineral. Petrol.* **1988**, *100*, 35–46. [[CrossRef](#)]
39. Leake, B.E.; Woolley, A.R.; Birch, W.D.; Burke, E.A.; Ferraris, G.; Grice, J.D.; Hawthorne, F.C.; Kisch, H.J.; Krivovichev, V.G.; Schumacher, J.C. Nomenclature of amphiboles: Additions and revisions to the International Mineralogical Association’s amphibole nomenclature. *Miner. Mag* **2004**, *68*, 209–215. [[CrossRef](#)]
40. Fleet, M.E.; Barnett, R.L. Al iv / Al vi partitioning in calciferous amphiboles from the Froid Mine, Sudbury, Ontario. *Can. Mineral.* **1978**, *16*, 527–532.
41. Tischendorf, G.; Förster, H.-J.; Gottesmann, B. The correlation between lithium and magnesium in trioctahedral micas: Improved equations for Li₂O estimation from MgO data. *Miner. Mag* **1999**, *63*, 57. [[CrossRef](#)]
42. Hey, M.H. A new review of the chlorites. *Mineral. Mag. J. Mineral. Soc.* **1954**, *30*, 277–292. [[CrossRef](#)]
43. Middlemost, E.A.K. Naming materials in the magma/igneous rock system. *Earth-Sci. Rev.* **1994**, *37*, 215–224. [[CrossRef](#)]
44. Irvine, T.N.; Baragar, W.R.A. A Guide to the Chemical Classification of the Common Volcanic Rocks. *Can. J. Earth Sci.* **1971**, *8*, 523–548. [[CrossRef](#)]
45. Sun, S.s.; McDonough, W.F. Chemical and isotopic systematics of oceanic basalts: Implications for mantle composition and processes. *Geol. Soc. Lond. Spec. Publ.* **2022**, *42*, 313–345. [[CrossRef](#)]
46. Abd El-Rahman, Y.; Seifert, T.; Gutzmer, J.; Said, A.; Hofmann, M.; Gärtner, A.; Linnemann, U. The South Um Mongul Cu-Mo-Au prospect in the Eastern Desert of Egypt: From a mid-Cryogenian continental arc to Ediacaran post-collisional appinite-high Ba-Sr monzogranite. *Ore Geol. Rev.* **2017**, *80*, 250–266. [[CrossRef](#)]
47. Munker, C.; Pfander, J.A.; Weyer, S.; Buchl, A.; Kleine, T.; Mezger, K. Evolution of planetary cores and the Earth-Moon system from Nb/Ta systematics. *Science* **2003**, *301*, 84–87. [[CrossRef](#)]
48. Ali, S.; Ntaflos, T.; Upton, B.G.J. Petrogenesis and mantle source characteristics of Quaternary alkaline mafic lavas in the western Carpathian–Pannonian Region, Styria, Austria. *Chem. Geol.* **2013**, *337–338*, 99–113. [[CrossRef](#)]
49. Polat, A.; Hofmann, A.W. Alteration and geochemical patterns in the 3.7–3.8 Ga Isua greenstone belt, West Greenland. *Precambrian Res.* **2003**, *126*, 197–218. [[CrossRef](#)]
50. Plank, T. Constraints from Thorium/Lanthanum on Sediment Recycling at Subduction Zones and the Evolution of the Continents. *J. Pet.* **2005**, *46*, 921–944. [[CrossRef](#)]
51. Taylor, S.R.; McLennan, S.M. The geochemical evolution of the continental crust. *Rev. Geophys.* **1995**, *33*, 241–265. [[CrossRef](#)]

52. Rudnick, R.L.; Gao, S. 3.01—Composition of the Continental Crust A2—Holland, Heinrich D. In *Treatise on Geochemistry*; Turekian, K.K., Ed.; Pergamon: Oxford, UK, 2003; pp. 1–64.
53. Miyashiro, A.; Shido, F. Tholeiitic and calc-alkalic series in relation to the behaviors of titanium, vanadium, chromium, and nickel. *Am. J. Sci.* **1975**, *275*, 265–277. [[CrossRef](#)]
54. Herzberg, C.; Asimow, P.D. Petrology of some oceanic island basalts: PRIMELT2.XLS software for primary magma calculation. *Geochem. Geophys. Geosyst.* **2008**, *9*. [[CrossRef](#)]
55. Wilson, M. *Igneous Petrogenesis*; Springer: Berlin/Heidelberg, Germany, 1989.
56. Yang, S.-H.; Zhou, M.-F. Geochemistry of the ~430-Ma Jingbulake mafic–ultramafic intrusion in Western Xinjiang, NW China: Implications for subduction related magmatism in the South Tianshan orogenic belt. *Lithos* **2009**, *113*, 259–273. [[CrossRef](#)]
57. Geng, H.; Sun, M.; Yuan, C.; Zhao, G.; Xiao, W. Geochemical and geochronological study of early Carboniferous volcanic rocks from the West Junggar: Petrogenesis and tectonic implications. *J. Asian Earth Sci.* **2011**, *42*, 854–866. [[CrossRef](#)]
58. Hofmann, A.W.; Jochum, K.P.; Seufert, M.; White, W.M. Nb and Pb in oceanic basalts: New constraints on mantle evolution. *Earth Planet. Sci. Lett.* **1986**, *79*, 33–45. [[CrossRef](#)]
59. Tang, Y.-J.; Zhang, H.-F.; Ying, J.-F. Asthenosphere–lithospheric mantle interaction in an extensional regime: Implication from the geochemistry of Cenozoic basalts from Taihang Mountains, North China Craton. *Chem. Geol.* **2006**, *233*, 309–327. [[CrossRef](#)]
60. Arndt, N.T.; Christensen, U. The role of lithospheric mantle in continental flood volcanism: Thermal and geochemical constraints. *J. Geophys. Res.* **1992**, *97*, 10967. [[CrossRef](#)]
61. Shahsavari Alavijeh, B.; Rashidnejad-Omran, N.; Toksoy-Köksal, F.; Chew, D.; Szopa, K.; Ghalamghash, J.; Gaweda, A. Geochemistry and apatite U–Pb geochronology of alkaline gabbros from the Nodoushan plutonic complex, Sanandaj–Sirjan Zone, Central Iran: Evidence for Early Palaeozoic rifting of northern Gondwana. *Geol. J.* **2019**, *54*, 1902–1926. [[CrossRef](#)]
62. Shaw, D.M. Trace element fractionation during anatexis. *Geochim. Et Cosmochim. Acta* **1970**, *34*, 237–243. [[CrossRef](#)]
63. McKenzie, D.; O’Nions, R.K. Partial Melt Distributions from Inversion of Rare Earth Element Concentrations. *J. Pet.* **1991**, *32*, 1021–1091. [[CrossRef](#)]
64. Aldanmaz, E.; Pearce, J.A.; Thirlwall, M.F.; Mitchell, J.G. Petrogenetic evolution of late Cenozoic, post-collision volcanism in western Anatolia, Turkey. *J. Volcanol. Geotherm. Res.* **2000**, *102*, 67–95. [[CrossRef](#)]
65. Pfänder, J.A.; Jung, S.; Münker, C.; Stracke, A.; Mezger, K. A possible high Nb/Ta reservoir in the continental lithospheric mantle and consequences on the global Nb budget—Evidence from continental basalts from Central Germany. *Geochim. Cosmochim. Acta* **2012**, *77*, 232–251. [[CrossRef](#)]
66. Zeng, G.; Chen, L.-H.; Xu, X.-S.; Jiang, S.-Y.; Hofmann, A.W. Carbonated mantle sources for Cenozoic intra-plate alkaline basalts in Shandong, North China. *Chem. Geol.* **2010**, *273*, 35–45. [[CrossRef](#)]
67. Salters, V.J.M.; Longhi, J.E.; Bizimis, M. Near mantle solidus trace element partitioning at pressures up to 3.4 GPa. *Geochem. Geophys. Geosyst.* **2002**, *3*, 1–23. [[CrossRef](#)]
68. Sisson, T.W.; Grove, T.L. Experimental investigations of the role of H₂O in calc-alkaline differentiation and subduction zone magmatism. *Contrib. Mineral. Petrol.* **1993**, *113*, 143–166. [[CrossRef](#)]
69. Condie, K. Changing tectonic settings through time: Indiscriminate use of geochemical discriminant diagrams. *Precambrian Res.* **2015**, *266*, 587–591. [[CrossRef](#)]
70. Blundy, J.D.; Robinson, J.A.C.; Wood, B.J. Heavy REE are compatible in clinopyroxene on the spinel lherzolite solidus. *Earth Planet. Sci. Lett.* **1998**, *160*, 493–504. [[CrossRef](#)]
71. Wang, K.; Plank, T.; Walker, J.D.; Smith, E.I. A mantle melting profile across the Basin and Range, SW USA. *J. Geophys. Res. Solid Earth* **2002**, *107*, ECV 5-1–ECV 5-21. [[CrossRef](#)]
72. O’Neill, H.S.C. The transition between spinel lherzolite and garnet lherzolite, and its use as a Geobarometer. *Contrib. Mineral. Petrol.* **1981**, *77*, 185–194. [[CrossRef](#)]
73. Abdel-Karim, A.-A.M.; Ali, S.; Helmy, H.M.; El-Shafei, S.A. A fore-arc setting of the Gerf ophiolite, Eastern Desert, Egypt: Evidence from mineral chemistry and geochemistry of ultramafites. *Lithos* **2016**, *263*, 52–65. [[CrossRef](#)]
74. Abdel-Karim, A.-A.M.; Ali, S.; El-Shafei, S.A. Mineral chemistry and geochemistry of ophiolitic metaultramafics from Um Halham and Fawakhir, Central Eastern Desert, Egypt. *Int. J. Earth Sci.* **2018**, *107*, 2337–2355. [[CrossRef](#)]
75. Ali, K.A.; Azer, M.K.; Gahlan, H.A.; Wilde, S.A.; Samuel, M.D.; Stern, R.J. Age constraints on the formation and emplacement of Neoproterozoic ophiolites along the Allaqi–Heiani Suture, South Eastern Desert of Egypt. *Gondwana Res* **2010**, *18*, 583–595. [[CrossRef](#)]
76. Kröner, A.; Krüger, J.; Rashwan, A.A.A. Age and tectonic setting of granitoid gneisses in the Eastern Desert of Egypt and south-west Sinai. *Geol. Rundsch.* **1994**, *83*, 502–513. [[CrossRef](#)]
77. Meert, J.G. A synopsis of events related to the assembly of eastern Gondwana. *Tectonophysics* **2003**, *362*, 1–40. [[CrossRef](#)]
78. Gahlan, H.A.; Obeid, M.A.; Azer, M.K.; Asimow, P.D. An example of post-collisional appinitic magmatism with an arc-like signature: The Wadi Nasb mafic intrusion, north Arabian–Nubian Shield, south Sinai, Egypt. *Int. Geol. Rev.* **2017**, *60*, 865–888. [[CrossRef](#)]
79. Winchester, J.A.; Floyd, P.A. Geochemical discrimination of different magma series and their differentiation products using immobile elements. *Chem. Geol.* **1977**, *20*, 325–343. [[CrossRef](#)]

80. Fan, W.-M.; Guo, F.; Wang, Y.-J.; Zhang, M. Late Mesozoic volcanism in the northern Huaiyang tectono-magmatic belt, central China: Partial melts from a lithospheric mantle with subducted continental crust relicts beneath the Dabie orogen? *Chem. Geol.* **2004**, *209*, 27–48. [[CrossRef](#)]
81. Biermanns, L. Chemical classification of gabbroic-dioritic rocks, based on TiO₂, SiO₂, FeO tot, MgO, K₂O, Y and Zr. In *Géodynamique Andine: Résumé Étendus = Andean Geodynamics: Extended Abstracts; Colloques et Séminaires*; ORSTOM: Paris, France, 1996; pp. 547–550.
82. Song, S.; Wang, M.; Wang, C.; Niu, Y. Magmatism during continental collision, subduction, exhumation and mountain collapse in collisional orogenic belts and continental net growth: A perspective. *Sci. China Earth Sci.* **2015**, *58*, 1284–1304. [[CrossRef](#)]
83. Sami, M.; Ntaflos, T.; Farahat, E.S.; Mohamed, H.A.; Hauzenberger, C.; Ahmed, A.F. Petrogenesis and geodynamic implications of Ediacaran highly fractionated A-type granitoids in the north Arabian-Nubian Shield (Egypt): Constraints from whole-rock geochemistry and Sr-Nd isotopes. *Lithos* **2018**, *304–307*, 329–346. [[CrossRef](#)]
84. Blasband, B.; White, S.; Brooijmans, P.; De Boorder, H.; Visser, W. Late Proterozoic extensional collapse in the Arabian–Nubian Shield. *J. Geol. Soc.* **2022**, *157*, 615–628. [[CrossRef](#)]
85. Abdel Halim, A.H.; Helmy, H.M.; Abd El-Rahman, Y.M.; Shibata, T.; El Mahallawi, M.M.; Yoshikawa, M.; Arai, S. Petrology of the Motaghairat mafic–ultramafic complex, Eastern Desert, Egypt: A high-Mg post-collisional extension-related layered intrusion. *J. Asian Earth Sci.* **2016**, *116*, 164–180. [[CrossRef](#)]

Disclaimer/Publisher’s Note: The statements, opinions and data contained in all publications are solely those of the individual author(s) and contributor(s) and not of MDPI and/or the editor(s). MDPI and/or the editor(s) disclaim responsibility for any injury to people or property resulting from any ideas, methods, instructions or products referred to in the content.